Digest Journal of Nanomaterials and Biostructures Vol. 20, No. 4, October-December 2025, p. 1407-1424

Visible-light-driven photocatalysis using g-C_3N_4 based ternary composite: a synergistic approach for effective degradation of organic pollutant

F. Attiq [a], K. M. Katubi [b], M. N. Khan [c], S. Zafar [a], I. Boukhris [d], M. S. AL-Buriahi [e], I. Shakir [c,f,*], M. Akhtar [a,*]

[a] *Department of Chemistry, The Govt. Sadiq College Women University Bahawalpur, Bahawalpur-63100, Pakistan*

[b] *Department of Chemistry, College of Science, Princess Nourah bint Abdulrahman University, P.O. Box 84428, Riyadh 11671, Saudi Arabia*

[c] *Department of Physics, Faculty of Science, Islamic University of Madinah, Madinah 42351, Saudi Arabia*

[d] *Department of Physics, Faculty of Science, King Khalid University; P.O. Box 9004, Abha; Saudi Arabia*

[e] *Department of Physics, Sakarya University, Sakarya, Turkey*

[f] *Sustainability Research Center, Islamic University of Madinah, Madinah, 42351, Saudi Arabia*

The widespread pollution of water resources by synthetic dyes and aromatic compounds has become a critical environmental challenge. To address this, we developed a novel photocatalyst, g-C_3N_4-modified ZnO/La_2O_3 nanocomposite, engineered for effective degradation of methylene blue (MB) dye and benzoic acid under visible light irradiation. The material's physical and optical properties were evaluated through XRD and UV–Visible spectroscopy, revealing its crystalline integrity and strong light absorption behavior. Under visible light illumination, the composite achieved promising degradation rates of over 90% for methylene blue and 68% for benzoic acid within 120 minutes. Compared to the binary ZnO/La_2O_3 system, the g-C_3N_4 enhancement significantly improved charge separation and broadened the absorption spectrum, resulting in faster reaction kinetics. The calculated rate constants were 0.01813 min^{-1} for MB and 0.0213 min^{-1} for BA. The photocatalyst maintained its performance across multiple reuse cycles, demonstrating excellent stability. Mechanistic studies identified electrons, holes, and hydroxyl radicals as key reactive species in the photodegradation reaction. Additional tests, including pH variation and measurement of total organic carbon (TOC), verified the material's adaptability and mineralization capability. These findings position g-C_3N_4@ZnO/La_2O_3 as sustainable solution for wastewater treatment technologies.

(Received August 3, 2025; Accepted November 6 ,2025)

Keywords: Ternary nanocomposite, Graphitic carbon nitride, Organic pollutants, Dye removal, Light-driven catalysis, Environmental remediation

1. Introduction

Organic pollutants in water sources are becoming increasingly prevalent worldwide as the population grows, along with the expansion of agricultural and industrial sectors [1]. Heavy metals, organic and inorganic pollutants present in industrial effluents, such as pesticides, phenols, dyes, and mineral acids, are harmful to aquatic life, plant diversity, and human health. Dyes, classified as the most common contaminant in textile wastewater, are one of the organic chemicals that chemically bind to the surface of the garment, thereby coloring it. It is easily detectable even at near-detectable levels (<1 ppm) and has potentially harmful effects [2]. Many dyes are harmful and may pose carcinogenic risks, making their elimination from industrial wastewater a significant environmental challenge.

* Corresponding author: mehwish.akhtar@gscwu.edu.pk

https://doi.org/10.15251/DJNB.2025.204.1407

To address this issue, several approaches have been proposed for removing dyes from water [3]. Degradation techniques are one of the useful methods that have been successfully used for dye removal from contaminated water among the various techniques, such as oxidation of synthetic dyes, coagulation, electrochemical process, surface adsorption phenomena, membrane separation, and biological process [4]. Each method has its advantages and limitations. Advanced oxidation processes, however, stand out as a promising area of research due to their effectiveness in degrading soluble organic pollutants from water and soil near ambient conditions, often achieving nearly complete breakdown [5].

Since the leading-edge study of Akira Fujishima and Kenichi Honda in 1972 on photoelectrochemical water-splitting via TiO_2, photocatalysis has come a long way and has become an inseparable component of advanced oxidation processes (AOPs). Complex waste materials, pollutants in high amounts, and poor biodegradability can be efficiently treated in wastewater using the method of photocatalysis. The novel strategy is not just energy-saving but also eco-friendly and feasible, and, therefore, a viable choice for sophisticated treatment of water with a sustainable resolution [1, 6]. Low-energy UV light is used in the process, and semiconductors serve as photocatalysts. In this approach, hazardous contaminants are degraded directly by electron-hole pairs produced by band-gap stimulation. While harmful metal ions can be reduced to metals and then recovered by solvent extraction, the holes serve as a potent oxidant to oxidize poisonous organic molecules [7]. Methylene blue ($C_{16}H_{18}N_3SC$), an aromatic cationic dye, is commonly used for dyeing various textiles. Nevertheless, about 40% of synthetic dyes are hazardous and carcinogenic chemicals. Such dyes tend to be persistent in industrial effluents, which is of great concern to the environment and human health [8, 9]. As a result, studies regarding innovative methods for the affordable mineralization of organic dyes are in progress.

Several metal oxides (MOs) are used to decompose organic contaminants present in industrial effluent. Nanostructured metal oxides possess distinctive features, including semiconducting and insulating behaviors [10], which make them suitable for several commercial and technological domains. MOs such as ZnO [11], TiO_2 [12], La_2O_3 [13], CeO_2 [14], MnO_2 [15], Gd_2O_3 [16], and so forth have been utilized for dye degradation. Zinc oxide nanoparticles (NPs) can be prepared cost-effectively by various chemical methods at relatively low temperatures, making it a practical choice for various applications. It absorbs in the ultraviolet region due to its high exciton binding. This property further adds to its usefulness for many applications in optics and photochemistry [17]. It became apparent that ZnO, having a band gap energy of 3.37eV, is a good substitute for TiO_2 and, in certain situations, is a more effective catalyst in the photodegradation process [18].

TiO_2 and ZnO are known to be extremely efficient photocatalysts for degrading many types of pollutants. Their high light sensitivity, chemical stability, and large band gap render them highly desirable for use in environmental remediation processes [19]. Nanostructured lanthanum oxide (nLa_2O_3) belongs to the class of p-type semiconductors and is a rare earth metal oxide with some unique chemical and physical characteristics, such as electrochemical inertia, excellent stability, high surface area, ecological sustainability, and its capability to interact with chemicals [20]. Lanthanum oxide (La_2O_3), with its broad energy band gap ($E_g > 4$ eV), low lattice energy, and high dielectric constant ($\epsilon = 27$ pF/m), is a promising rare-earth oxide for photocatalytic processes. Its special characteristics make it a very valuable semiconductor for various optical and electrical applications [21]. The large band gap of La_2O_3 improves the characteristics of zinc oxide by generating new energy states within the band gap, as revealed by Evans (2013). Moreover, lanthanum oxide's low cost highlights its great potential for large-scale commercial uses [22].

The remarkable characteristics of g-C_3N_4-based materials, such as their high stability, non-toxicity, ease of synthesis, affordability, as well as their capacity to absorb visible light, have prompted growing interest over the last few decades [23]. It is an incredible material having numerous potential uses in the energy and environmental domains, like photovoltaics [24], sensing [25, 26], and photocatalysis [27-29]. Due to its quick emission, strong excitation binding energy, and band gap energy (E_g) of 2.7 eV [30], g-C_3N_4 frequently exhibits high-yield luminescence. However, a modification must be made to g-C_3N_4 either by coupling or doping with other semiconductor materials (metals/non-metals) to reduce the likelihood of electron and hole pairs recombining [27, 30, 31], poor quantum yield, and an inadequate specific surface area [32, 33].

Inspired by the facts provided above, a novel g-C_3N_4 doped ZnO/La_2O_3 catalyst was fabricated by a facile wet precipitation and ultrasonication was applied for loading g-C_3N_4. In contrast to other approaches, the wet precipitation method for the synthesis of nanomaterials constitutes numerous benefits, notably high-quality materials, cheap processing costs, a relatively low temperature, and an excellent yield [10]. Following similar events and parameters, g-C_3N_4 was introduced into a ZnO/La_2O_3 framework. Techniques like XRD and FTIR were used for analyzing the prepared nanomaterials. To evaluate the degradation efficiency of the fabricated catalysts, degradation MB dye and benzoic acid was conducted under visible light irradiation.

2. Methodology and characterization

2.1. Chemicals

Chemicals including lanthanum nitrate hexahydrate, ammonium chloride, acetone, absolute ethanol, benzoic acid, and methylene blue were purchased from Sigma Aldrich, zinc nitrate hexahydrate from ACS Chemicals, while melamine and sodium hydroxide from Emparta. Since all the chemicals and reagents used in this study are almost 99.8 % pure and used as received.

2.2. Fabrication of ZnO/La_2O_3 Binary Nanocomposite

ZnO and La_2O_3 nanopowders were synthesized by using the co-precipitation method [34, 35]. The as-prepared ZnO and La_2O_3 nanopowders were combined in a 1:1 weight ratio and thoroughly ground to ensure precise and effective mixing. The ZnO/La_2O_3 combination was then dissolved in distilled water and sonicated for about 2 hours, resulting in a homogeneous solution. After that, the resultant mixture was dried in a vacuum oven set at 80°C and later annealed at 450°C for 2 hours to obtain nanopowder.

2.3. Fabrication of Graphitic Carbon Nitride (g-C_3N_4)

10 g of melamine was heated in an alumina crucible by placing it in a muffle furnace set at 500 ºC for 2 hours, having a heating rate of 20 ºC min^{-1}. A yellowish powder was obtained as a product after cooling [36][37].

To prepare g-C_3N_4 nanorods, the previous method was used [38]. In a conventional reaction, 2.8 mmol of NH_4Cl was mixed in 20 cm^3 of double-distilled water. A 0.5 mmol bulk g-C_3N_4 solution was also prepared and mixed into the ammonium chloride solution prepared earlier, followed by uniform stirring for half an hour. Sonication was applied to the suspension for 30 minutes. This suspension was poured into a 25 cm^3 Teflon-lined autoclave and heated in the oven for 12 hours at 160 °C. After being brought to room temperature, the final product was centrifuged, washed, and dried for 12 hours at 50 °C, as presented in Figure 1.

2.4. Fabrication of g-C_3N_4@ZnO/La_2O_3 Ternary Nanocomposite

80 mg of ZnO/La_2O_3 nanocomposite dissolved in distilled water was combined with 10 cm^3 of the previously synthesized g-C_3N_4 nanorods solution to yield the ternary nanocomposite. After 2 hours of ultrasonication and 60 °C oven drying, g-C_3N_4@ZnO/La_2O_3 nanopowder was obtained as shown in Figure 1.

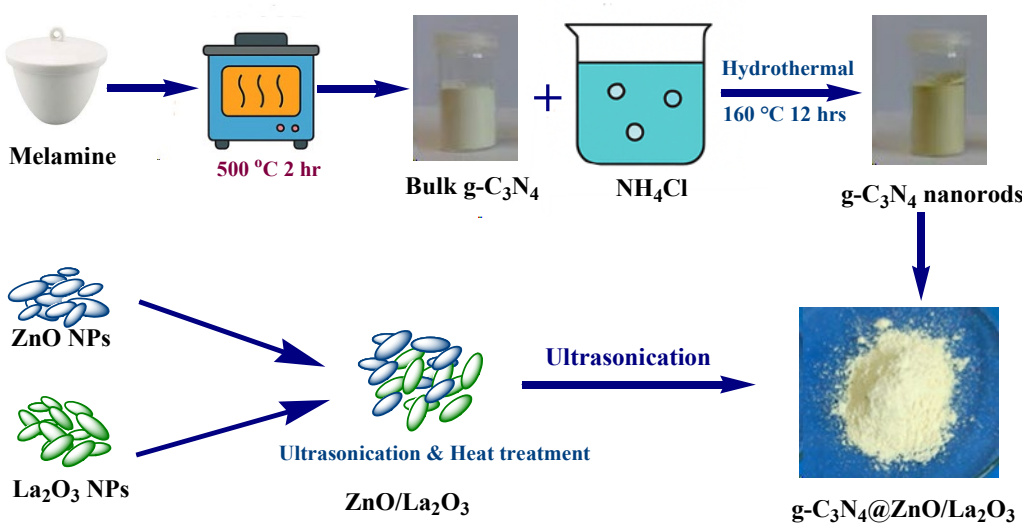

Fig. 1. Schematic diagram for the preparation of g-C_3N_4 nanorods and g-C_3N_4@ZnO/La_2O_3.

2.5. Characterization Instruments

To study the phase structure of the prepared catalysts, diffraction patterns were recorded using a 3040/60 diffractometer with Cu-K radiation (= 0.154 nm) facility (Philips X Pert PRO). With the help of a spectrophotometer (Nexus 470), FT-IR spectra were obtained for identifying different functional groups of the synthesized samples within range 4000-500 cm^{-1}. For the UV-visible analysis, Cary 60 UV-Visible double-beam spectrophotometer was utilized. Moreover, the morphological and elemental determination of the fabricated g-C_3N_4@ZnO/La_2O_3 was explored by FE-SEM using Zeiss Sigma VP 500 along with a Metek detector EDX.

3. Data Analysis and Discussion

3.1. Structural Analysis via XRD

X-ray diffractograms of binary ZnO/La_2O_3 and g-C_3N_4-doped ZnO/La_2O_3 nanocomposites are given in Figure 2. The samples showed prominent diffraction peaks for La_2O_3, ZnO, and g-C_3N_4. The XRD patterns show two consistent peaks generated by g-C_3N_4 nanorods. The tri-s-triazine unit peak, indexed as (100) diffraction plane with interplanar spacing 0.675 nm, correlates to the peak at 2Θ=15.74°. Moreover, the peak appearing at 2Θ=26.9°, which is designated as the (002) diffraction plane of the conjugated aromatic system, is related to the π-π stacking interactions of aromatic rings with an interplanar distance of 0.33 nm (Paul et al., 2020). The XRD pattern shows that there were no significant changes in the crystalline structure of g-C_3N_4 after following hydrothermal treatment with ammonium chloride [38]. Five strong peaks at 31.65°, 34.38°, 36.13°, 47.37°, and 56.25° in the ZnO/La_2O_3 XRD pattern were assigned to (100), (002), (101), (102), and (110) planes (JCPDS no. 36-1451) [39]. La_2O_3 occurs in both hexagonal and cubic phases. The hexagonal phase of La_2O_3 was responsible for the diffracted peaks at 2Θ = 30.28° (011), 39.28° (012), 44.48° (110), 48.79° (111), and 54.79° (112) whereas the cubic phase of La_2O_3 was responsible for 25.7° (211) and 27.29° (222) (Ikram et al., 2022). The composite g-C_3N_4@ZnO/La_2O_3 displayed two extra peaks at 2Θ = 15.74 ° (100) and 26.9° ° (002) in contrast to ZnO/La_2O_3, which implies the fabrication of g-C_3N_4 functionalized nanoparticles. Using Debye-Scherrer's formula, the crystallite size of the prepared catalysts was computed [40];

$$D = \frac{0.9\,\lambda}{\beta cos\theta} \quad (1)$$

where β is full-width at half maximum (FWHM), λ represents the wavelength of X-rays used, and θ represents the diffraction angles. These results indicates that g-C_3N_4-doped ZnO/La_2O_3 nanocomposites were successfully prepared.

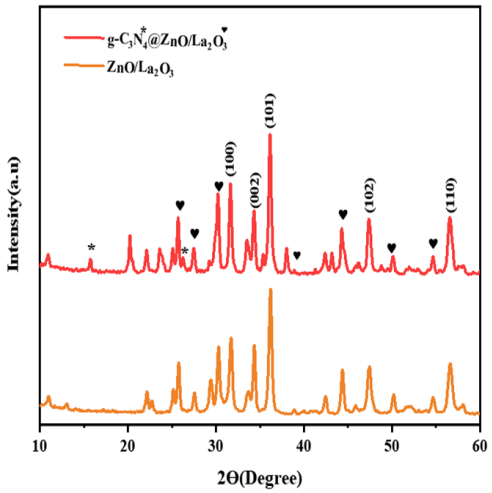

Fig. 2. XRD patterns of prepared nanocomposites.

3.2. FT-IR analysis

The spectra were observed in the frequency range of 500–4000 cm^{-1} as shown in Figure 3 (a). However, the zoomed FTIR spectra of ZnO/La_2O_3 and g-C_3N_4@ZnO/La_2O_3 nanocomposites showed the characteristic peaks as displayed in Figure 3 (b). The transmittance peak at 562 cm^{-1} is of MO (Zn-O stretching vibrations) vibration mode [41]. The transmittance peaks at 621, 853, and 1087 cm^{-1} are due to the stretching modes of La-O [42, 43]. While peaks at 1151 and 1358 cm^{-1} are ascribed to the OH bending vibrations. The 1461 cm^{-1} band may arise due to the absorption of atmospheric CO_2 [2].

For g-C_3N_4@ZnO/La_2O_3, the peak at 1610 cm^{-1} is attributed to the C=N stretching vibrations, while the peaks at 1241 cm^{-1}, 1318 cm^{-1}, and 1416 cm^{-1} are due to aromatic C-N stretching. The characteristic strong peak of g-C_3N_4 at 806 cm^{-1} is associated with the vibrational bending of the s-triazine ring [44]. Transmittance bands corresponding to ZnO, La_2O_3, and g-C_3N_4 can be seen in the nanocomposites. Thus, FTIR also confirmed the formation of g-C_3N_4@ZnO/La_2O_3.

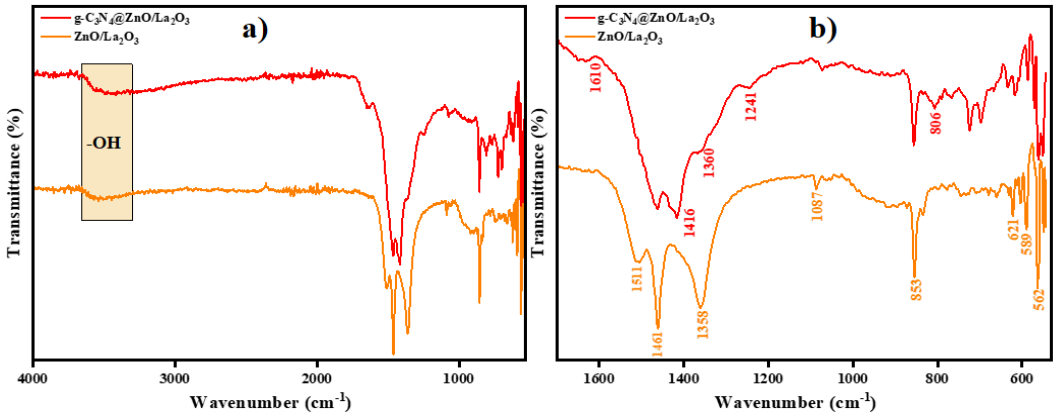

Fig. 3. FTIR spectra for ZnO/La_2O_3 and ZnO/La_2O_3/g-C_3N_4.

3.3. Optical Study via UV-visible Spectroscopy

The UV-visible spectra were used to study the optical properties of ZnO/La_2O_3 and g-C_3N_4@ZnO/La_2O_3 nanocomposites as shown in Figure 4. The binary nanocomposite ZnO/La_2O_3 displayed broad absorption bands from 280 nm to 400 nm, demonstrating favourable wavelength selectivity. A small shift in the absorption band edge was seen in g-C_3N_4@ZnO/La_2O_3, which may have been caused by interaction between the g-C_3N_4 component and the ZnO/La_2O_3 binary nanocomposite.

A material's capacity to produce electron-hole pairs during excitation is indicated by its band gap energy. The material's form, size, and proportions have a significant impact on this property. To find the band gap energy of the prepared samples, the Tauc relation was employed, which is expressed as [45]:

$$(\alpha h\nu)\ n = A\ (h\nu - Eg) \quad (2)$$

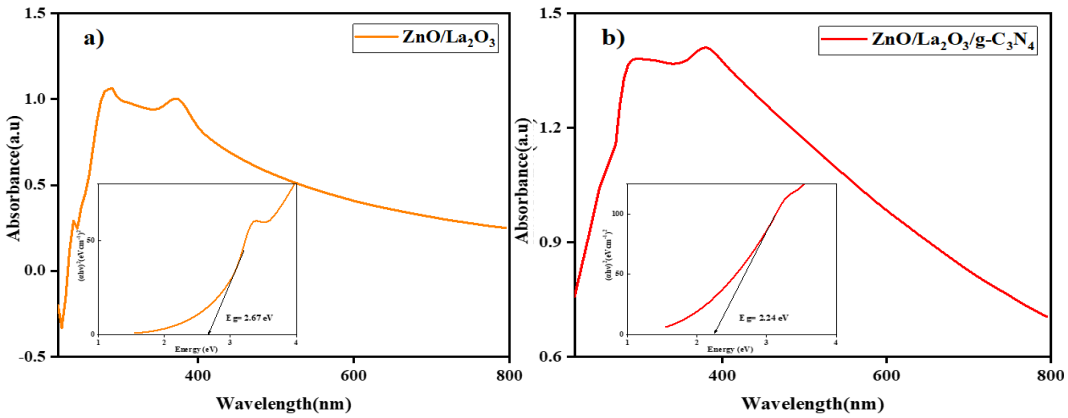

Fig. 4. Absorbance spectra and Tauc plots for ZnO/La_2O_3 and g-C_3N_4@ZnO/La_2O_3.

In the given equation, the symbol 'α' denotes the coefficient of absorption, 'h' represents Planck's constant, 'ν' stands for the vibrational frequency, 'E_g' indicates energy gap between conduction and valence bands, 'A' is a material-specific constant, and 'n' is a constant associated with electronic state transitions, including both direct (2) and indirect (1/2) ones. To ascertain the direct band gap, a graph was constructed, plotting $(\alpha h\nu)^2$ on the y-axis and energy on the x-axis. During photodegradation experiments, the efficient generation of electrons and holes hinges on the material's band gap energy. The ZnO/La_2O_3 binary nanocomposite exhibits about a 2.67 eV band gap energy, while the ternary nanocomposite g-C_3N_4-doped ZnO/La_2O_3 showcases 2.24 eV band gap. Due to a lower band gap value, g-C_3N_4@ZnO/La_2O_3 is capable of efficiently absorbing visible light, thereby enhancing the degradation efficiency of the material.

3.4. Scanning Electron Microscopy (SEM)

The morphology of the freshly fabricated photocatalytic material, i.e., g-C_3N_4@ZnO/La_2O_3, was evaluated by SEM. Figure 5 (a) shows the large number of very small particles, as the scale bar of 10 µm suggests the aggregation of smaller structures. The individual agglomeration of nanoparticles and sheets of g-C_3N_4, as exhibited in Figure 5 (b), presented irregular shapes and a wide range of sizes. Some particles and sheets appeared the loose packing, while others presented dense packing in the SEM as displayed in Figure 5 (c). The occurrence of tiny particles and their agglomeration suggested a higher surface area. Having a larger surface area is a desirable characteristic of the catalyst, it provides more active sites for effective adsorption of effluents leading to a higher rate of reaction. Moreover, the porous appearance facilitates the diffusion of wastewater contaminants to the catalytic sites present on the surface of model g-C_3N_4@ZnO/La_2O_3. The porosity and more catalytic sites enhance the mineralization ability of the photocatalytic materials [46].

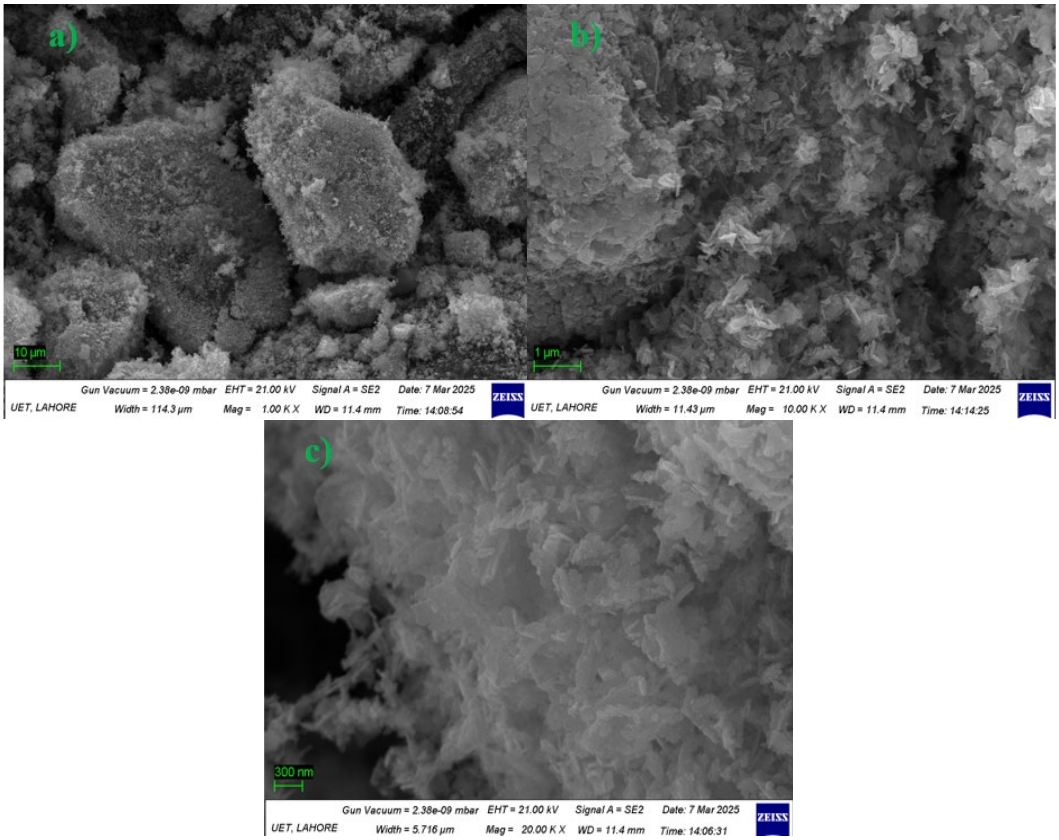

Fig. 5. SEM images of fabricated g-C_3N_4@ZnO/La_2O_3 at (a) 10 µm, (b) 1 µm, and (c) 300 nm.

3.5. Energy Dispersive X-ray (EDX) Spectroscopy

The existence of respective elements in the prepared photocatalysts was analysed via EDX. The EDX spectra of freshly prepared g-C_3N_4@ZnO/La_2O_3 are displayed in Figure 6. The peaks of respective elements are visible, which confirms their presence in the photocatalytic material. The absorption peaks of nitrogen (N), oxygen (O), and carbon (C) lie between 0.0 and 1.3 keV. However, lanthanum (La) and zinc (Zn) appear in the energy range of 3.9 and 9.1 keV. The calculated atomic percentage of C, N, O, La, and Zn was 7.64 %, 11.86 %, 47.05 %, 8.51 %, and 24.95 %, respectively. The presence of constituent elements affirms the formation of g-C_3N_4@ZnO/La_2O_3.

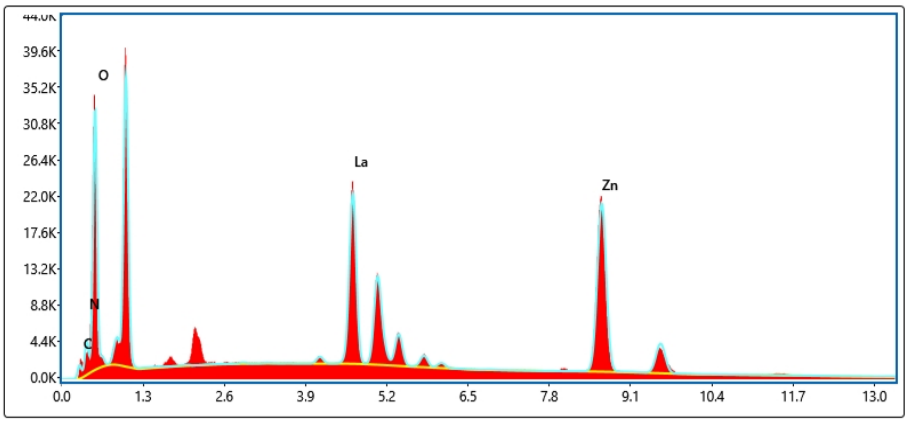

Fig. 6. EDX profile of fabricated g-C_3N_4@ZnO/La_2O_3.

3.6. Photodegradation Experiment

To study the catalytic potential of the fabricated photocatalysts, i.e., ZnO/La_2O_3 and g-C_3N_4@ZnO/La_2O_3, methylene blue, an organic-colored dye, and benzoic acid, a colorless effluent, were exposed to photocatalytic degradation under visible light. When subjected to visible light (420 nm), degradation tests were carried out using a tungsten filament commercial bulb (200 W). The light source was monochromatic. The lamp and photocatalytic reactor were kept 4 cm apart. In a standard experimental setup, for the preparation of a 5 ppm MB solution, 5 mg of a colored dye was mixed in 1000 cm^3 of distilled water. For benzoic acid, a 50 ppm solution was prepared. Then, 20 mg of binary ZnO/La_2O_3 and ternary g-C_3N_4@ZnO/La_2O_3 photocatalysts were added to 50 cm^3 of the pre-prepared solutions with the dye and benzoic acid. The obtained mixture was left in the dark and mixed repeatedly at room temperature. After an interval of 30 minutes, a sample of 4 cm^3 was drawn out from the solution at the start time and centrifuged for 10 minutes at 2000 revolutions per minute, separating the catalyst from the sample. The absorbance spectra were then recorded via a UV-visible spectrophotometer. In the presence of a photocatalyst, the solution was illuminated with visible light under a lamp to cause the degradation of the dye. Absorbance measurements were done at 15-minute intervals to observe the degradation rate.

3.6.1. Photocatalytic Activity of Methylene Blue

When exposed to visible light, the photodegradation efficacy of ZnO/La_2O_3 and g-C_3N_4@ZnO/La_2O_3 catalysts towards methylene blue were investigated. During the photocatalysis reaction, the surface reactivity of the photocatalyst against dye adsorption is crucial. Figure 7 depicts the absorption spectra of methylene blue dye in the presence of ZnO/La_2O_3 and g-C_3N_4@ZnO/La_2O_3. While the absorption at time 0 min demonstrated the ability of various photocatalysts to absorb in the dark, the absorption spectra observed after a certain period demonstrate a reduction in peak intensities of the dye. In comparison to the ZnO/La_2O_3 binary composite, the g-C_3N_4@ZnO/La_2O_3 outlined improved degradation potential, due to higher surface area of the as-prepared material. The photocatalytic degradation efficiency of the MB dye is in the following order: g-C_3N_4@ZnO/La_2O_3 (90.38%) > ZnO/La_2O_3 (86.53%).

A lower band gap and the highest surface area as a result of doping g-C_3N_4 nanorods with ZnO/La_2O_3 matrix are due to the highest degradation performance of g-C_3N_4@ZnO/La_2O_3 nanocomposite. The incorporation of ZnO/La_2O_3 into g-C_3N_4 effectively enhances the nano photocatalyst's surface area, leading an increased number of active sites for adsorption and heightened surface activity concerning dyes. The %age degradation efficacy was determined using the relation given below [47] [48].

$$\text{Photodegradation efficacy (\%)} = \left[1 - \frac{C_t}{C_0}\right] \times 100 \tag{3}$$

The kinetics of the photodegradation of MB dye can potentially be exploited to study the catalytic activity of ZnO/La_2O_3 binary and g-C_3N_4@ZnO/La_2O_3 ternary photocatalysts. Further, the rate constant (k) value for dye degradation was determined using pseudo-first-order kinetics for each photocatalytic experiment to do further studies on the degradation reaction [49].

$$kt = -\ln\left[\frac{Ct}{Co}\right] \tag{4}$$

where C_t/C_o is ratio of concentration of MB at time=t to its initial concentration of the dye at time= 0 minutes, k indicates the rate constant value, and t is the period of irradiation. Straight-line graphs were generated when data were plotted between time and -ln(C_t/C_o). Pseudo-first-order kinetics are implied by linear graphs of -ln(C_t/C_o) versus time (t) for the sample. Figure 8 exhibits the rate constant and %age degradation values for MB dye utilizing various photocatalysts, with values increasing in the order that is given: g-C_3N_4@ZnO/La_2O_3 > ZnO/La_2O_3. The maximum photocatalytic rate constant value was obtained by utilizing g-C_3N_4@ZnO/La_2O_3 nanocomposites. The results of the study for the % MB degradation kinetics parameters, linear regression coefficient, and pseudo-first-order degradation rate constant (K) are shown in Table 1.

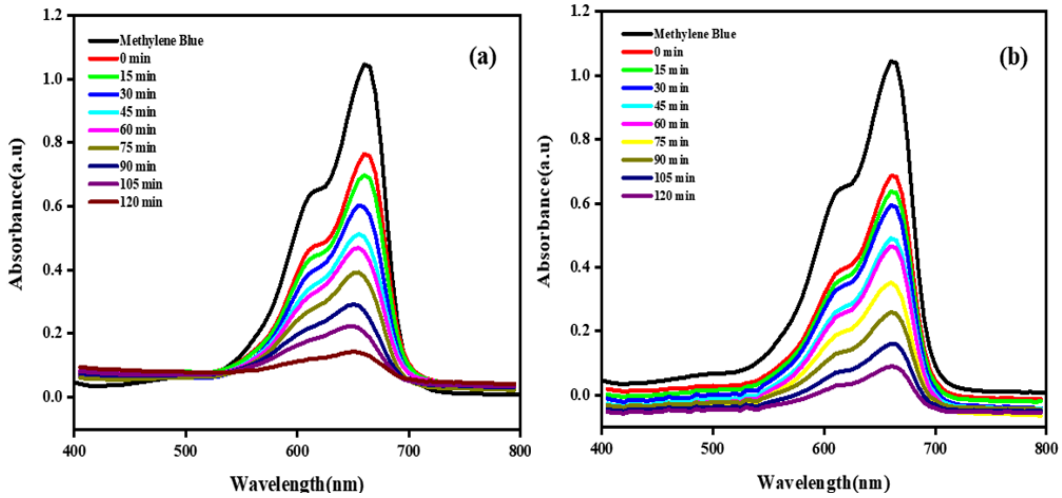

Fig. 7. UV-visible absorbance spectra of methylene blue dye degradation by (a) ZnO/La_2O_3 and (b) g-C_3N_4@ZnO/La_2O_3 nanocomposite.

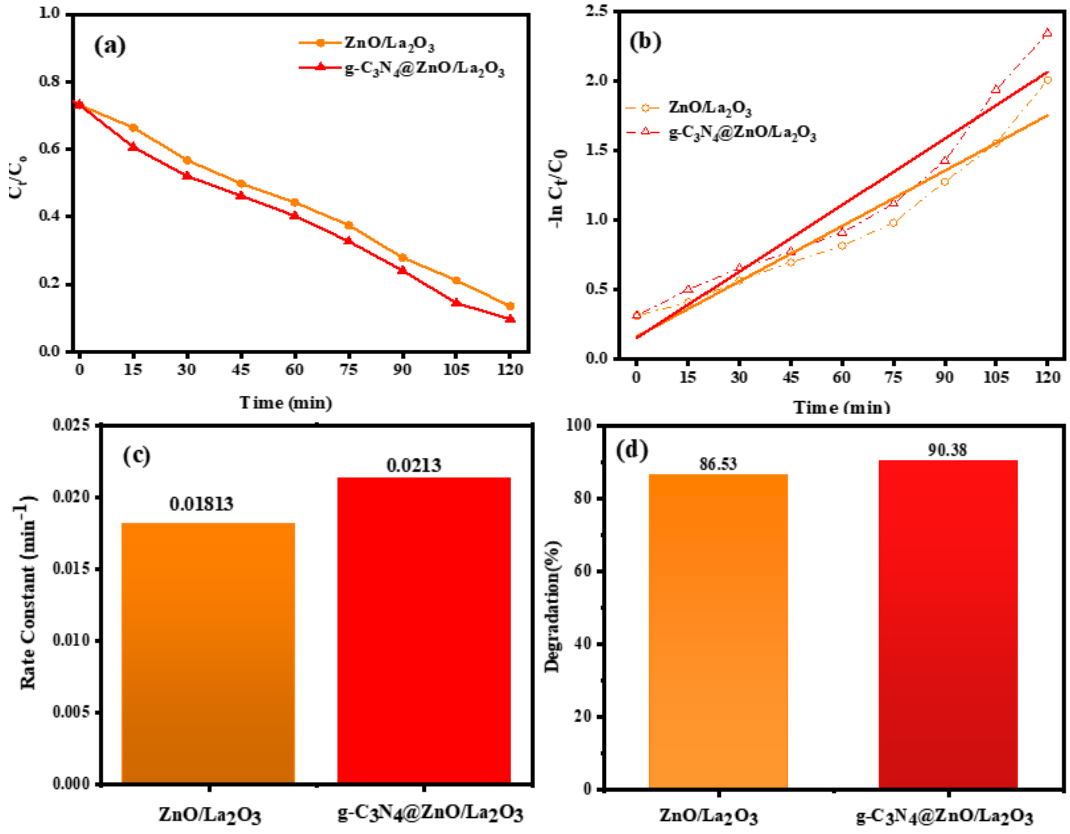

Fig. 8. Kinetic analysis of photodegradation of MB (a) A kinetic plot illustrating the photodegradation of the dye. (b) A plot of the relationship of –ln (C_t/C_0) with time (c), an increase in the rate constant (k) value when exposed to light, and (d) Percent degradation efficiency of methylene blue in the existence of g-C_3N_4@ZnO/La_2O_3 photocatalysts after 120 min.

Table 1. The kinetics parameters for percentage MB degradations, linear regression coefficient, and rate constant (k).

Photocatalyst	**Amount of Catalyst (mg)**	**Reaction Time (min)**	**Degradation Efficiency (%)**	**k (min^{-1})**	**R^2**
ZnO/La_2O_3	120	20	86.53	0.01813	0.9323
g-C_3N_4@ZnO/La_2O_3	120	20	90.38	0.0213	0.9002

3.6.2. Photocatalytic Activity of Benzoic Acid

Upon exposure to visible light, the photocatalytic efficiency of g-C_3N_4@ZnO/La_2O_3 nanocomposites towards benzoic acid was investigated. The results have been displayed in Figure 9. The specific absorbance peak of benzoic acid was found at 230 nm. The progressive shift in BA peak intensities at periodic time intervals indicates degradation. At 0 minutes, the absorption indicated the photocatalysts' capacity to function in darkness, influenced by their extensive surface area and low band gap energy, result

ing from doping g-C_3N_4 nanorods with ZnO/La_2O_3 matrix is attributed to the highest degradation performance of g-C_3N_4@ZnO/La_2O_3 nanocomposite.

Figure 10. illustrates the kinetic profiles and degradation percentages concerning benzoic acid across different time intervals. The g-C_3N_4@ZnO/La_2O_3 photocatalyst accomplished a degradation rate of approximately 68.34% after 120 minutes in the case of benzoic acid. The rate constant for benzoic acid was calculated through a straight line of $-\ln(C_t/C_o)$ against time as 0.00816 min^{-1} with the utilization of the g-C_3N_4@ZnO/La_2O_3 photocatalyst. Table 3 offers a comparison of degradation percentages among various photocatalysts in the context of diverse dye removal scenarios.

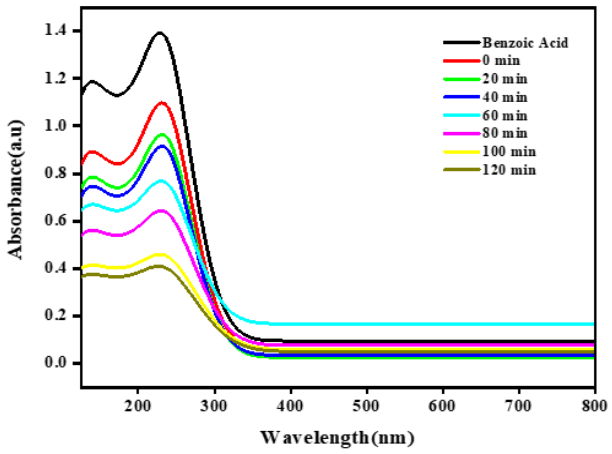

Fig. 9. UV-visible spectra for the degradation of benzoic acid by g-C_3N_4@ZnO/La_2O_3 nanocomposite.

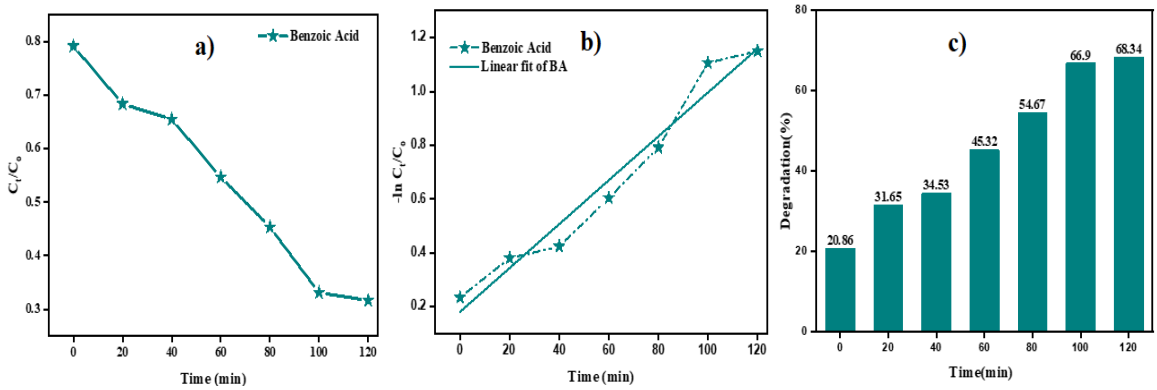

Fig. 10. (a) Kinetic plots of g-C_3N_4@ZnO/La_2O_3 for benzoic acid degradation (b) -ln (C_t/C_0) plots against time (c) Comparative photodegradation percentage of BA in the presence of g-C_3N_4@ZnO/La_2O_3 photocatalyst at different intervals of time.

Table 2. The BA Percentage degradation kinetics parameters, rate constant (k) and the adj-R^2.

Photocatalyst	**Reaction Time (min)**	**Amount of Catalyst (mg)**	**Degradation Efficiency (%)**	**k (min^{-1})**	**R^2**
g-C_3N_4@ZnO/La_2O_3	120	20	68.34	0.00816	0.9545

Table 3. Comparison of previously reported percent degradation efficiency for the removal of various dyes using various photocatalysts.

Photocatalysts	**Azo Dye**	**Light Source**	**Reaction Time (min)**	**Degradation Efficiency (%)**	**Reference**
La_2O_3 NPs	MG	UV	120	87.32	[50]
Mn@ZnO	MB	UV	35	~77	[51]
ZnO-La_2O_3	MB	UV	120	81.75	[52]
g-C_3N_4/ZnO	MB	UV	360	~90	[53]
In_2O_3/OGCN	BPA	Xe lamp	180	91	[54]
ZnO/ZnS/g-C_3N_4	MB	Visible	70	98.39	[55]
$CoFe_2O_4$/g-C_3N_4/ZnO	MB	Visible	100	89	[56]
GaN-ZnO/g-C_3N_4	MB	Visible	300	98.1	[57]
ZnO.La_2O_3.CeO_2	RhB	Mercury vapor lamp	160	94.99	[13]
La_2O_3–CoO–g-C_3N_4	MB	Xe lamp	360	~90	[58]
ZnO/La_2O_3	MB	Visible	120	86.53	This work
g-C_3N_4@ZnO/La_2O_3	MB, BA	Visible	120	90.38,68.34	This work

3.6.3. Scavenging Experiment

Experiments were done to assess the role of various reactive species/radicals during the degradation of MB, utilizing the active species produced by g-C_3N_4@ZnO/La_2O_3 under visible light. By utilizing numerous free radical trapping substances including ascorbic acid (AA) (0.25 mM), ammonium oxalate (AO) (1 mM), and 2-butanol (2-B) (0.13 mM), it is possible to determine the roles of hydroxyl radical, holes, and electrons in the photodegradation process. ascorbic acid, ammonium oxalate and 2-butanol were used as chemical traps for $O_2^{-\bullet}$, $h^{+\cdot}$ and $OH^{\cdot}$, respectively. During the photodegradation of an organic dye (methylene blue), these scavengers serve to track the inhibitory effect. The degradation percentage outcomes for scavenging investigations are shown in

Figure 11. The inclusion of scavengers led to a decrease in degradation percentages by 67.7% for ascorbic acid, 58.09% for ammonium oxalate, and 39.82% for 2-butanol, respectively. The overall results of the experiments demonstrate that the presence of trapping agents decreases photodegradation of MB, which somewhat underlines the importance of hydroxyl radicals, holes and electrons in the entire photodegradation investigations. When MB dye is degraded by g-C_3N_4@ZnO/La_2O_3 photocatalyst, the order of the active species is OH^* > h^+ > $O_2^{-\bullet}$. The percent degradation and rate constant findings demonstrate the substantial role of OH^* in the redox processes throughout the entire catalytic process, and 2-butanol as a hydroxyl radical quencher causes the photocatalytic organic dye degradation to decrease to a greater extent. Consequently, it is the dominant inhibitor specie.

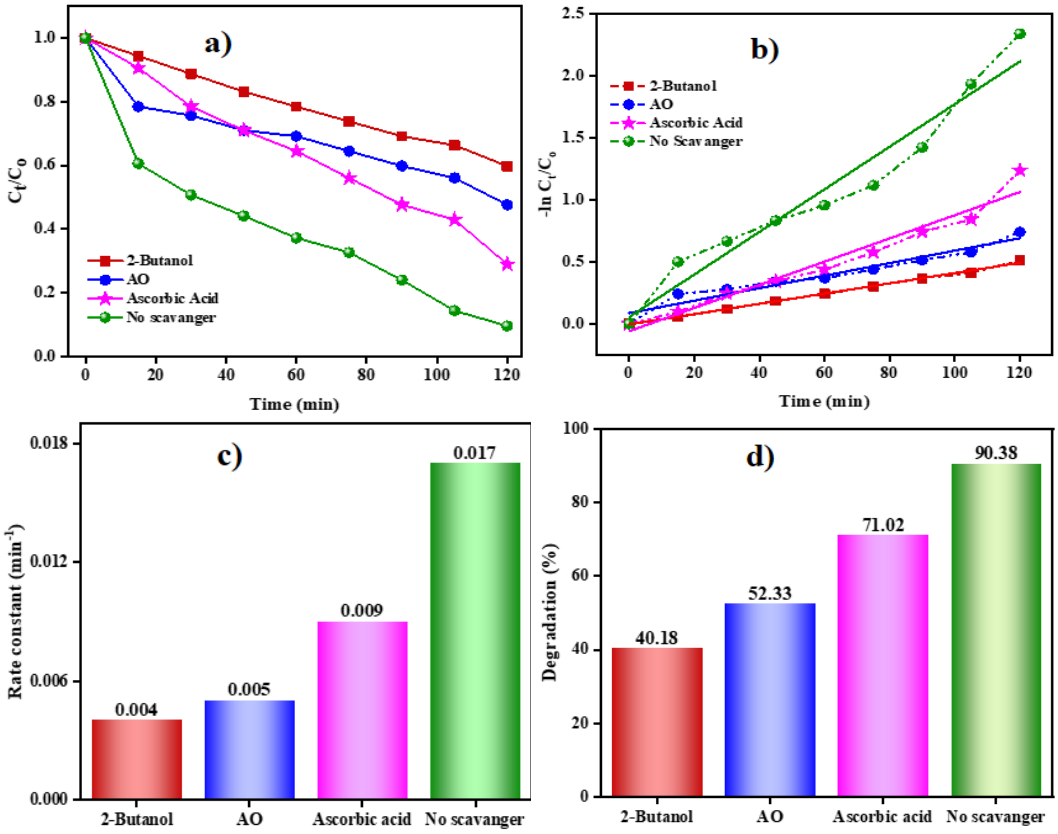

Fig. 11. Kinetic plots, rate constant, and percentage degradation for the photodegradation of MB under various scavengers.

3.6.4. Effect of pH

The solution's pH directly influences the mineralization rate of the contaminants. This influence may arise due to the variations in molecular structure, ionization state, and surface properties of dyes and photocatalytic materials. The photocatalyst's surface displays the pH-dependent charge characteristics, where acidic conditions enhance H^+ ion adsorption, resulting in a positively charged surface, while under alkaline conditions, the catalyst adsorbs more OH^- ions, leading to a negative surface charge. The photodegradation of pollutants, i.e., MB (cationic dye) and BA (anionic compound), was tested by using g-C_3N_4@ZnO/La_2O_3 in acidic and alkaline media. To investigate how pH affects the degradation percentage, the solution's pH was set using a 0.1M solution of HCl and NaOH. The ability to mineralize MB and BA was assessed over a pH ranging from 4-10, given in Figure 12. The percentage degradation was increased (74.8 % and 65.91 %) up to pH = 7 and 6 for MB and BA. The charge on the catalyst's surface at this pH allowed optimal adsorption and degradation of the pollutants. Furthermore, it was noticed that the percentage

degradation was decreasing after the optimal pH, as displayed in Figure 12 (a) and (b). The higher percentage degradation at pH 7 and 6 for MB and BA can be possible due to the stronger electrostatic forces occurring between methylene blue and freshly fabricated g-C_3N_4@ZnO/La_2O_3.

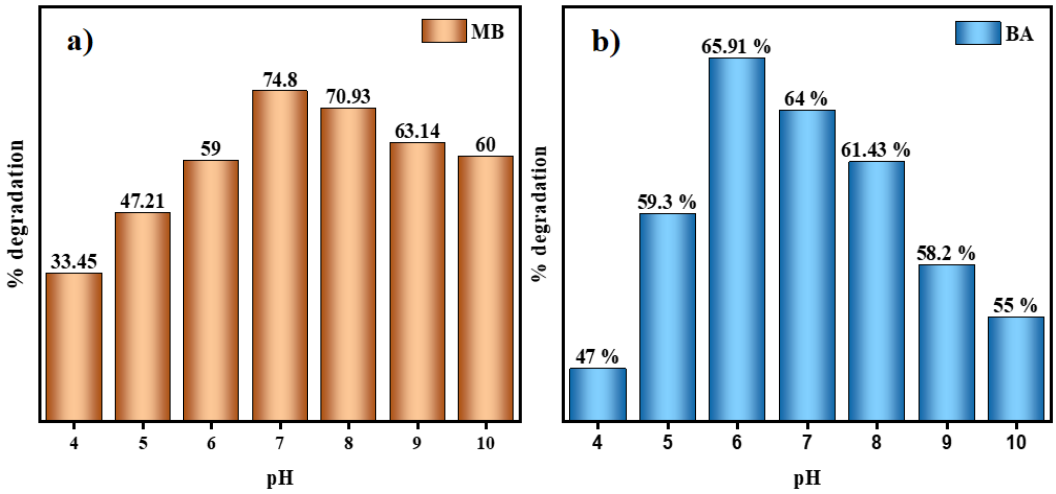

Fig. 12. Effect of pH using g-C_3N_4@ZnO/La_2O_3 on the photodegradation (a) MB and (b) BA.

3.6.5. TOC measurements

The photo-degradation efficacy of the prepared photocatalysts, specifically g-C_3N_4@ZnO/La_2O_3, was evaluated through the mineralization of MB, a model contaminant. Total organic content (TOC) measurements were used to observe the process of degradation. Measurements of TOC were performed by preparing the MB solution in COD vials and adding the catalyst, i.e., g-C_3N_4@ZnO/La_2O_3. Furthermore, potassium acid solution and distilled water were used for making standard and blank solutions. The volume of the three solutions was the same as $3cm^3$. After that, all the vials were settled for incubation at 120 °C for 120 minutes. At last, the TOC was measured by a COD meter. The photocatalytic mineralization of MB was determined by determining the total organic carbon removal in the presence of g-C_3N_4@ZnO/La_2O_3. The total organic carbon removal was calculated using equation 5 and found to be 88.53 % for MB. This suggests that practically all of the contaminants were converted into water and carbon dioxide, two simple molecules.

$$\text{TOC (\% age removal)} = \frac{\boldsymbol{TOC\ (untreated) - TOC\ (treated)}}{\boldsymbol{TOC\ (untreated)}} \times \mathbf{100} \quad (5)$$

3.6.6. Photocatalytic Mechanism

The degradation process can be clarified by investigating the relation between photocatalytic activity and the adsorption capacity of ZnO/La_2O_3 in conjunction with g-C_3N_4. The fundamental mechanism of photo-degradation begins when UV-visible light interacts with the combination of the dye and photocatalyst, as depicted in Figure 13. Consequently, the photocatalyst absorbs the high-energy photons, resulting in photo-excitation and the e^-/h^+ pairs throughout the photocatalyst's surface (Equations 6-8). These generated excitons play a critical role in the reduction of organic contaminants via redox reactions. As the photogenerated electrons consume the adsorbed oxygen, they reduce it to superoxide radicals (Equation 9). These superoxide radicals then react with water molecules, yielding hydroxyl ions and peroxide radicals (Equation 10). The highly reactive hydroxyl radical can also be produced when the peroxide radical anion reacts with H_2O (Equation 11) or when hydrogen peroxide reacts with electrons (Equation 12). The hydroxyl radical, which is primarily formed by the conduction band electrons, serves as the primary agent to degrade organic contaminants, transforming them into mineralized organic composites. Most notably, the highly reactive hydroxyl radical is generated either through the breakdown of water molecules upon

interaction with holes [59, 60] (Equation 13). The overall mechanism of the reaction may be summarized as follows:

$$g\text{-}C_3N_4@ZnO/La_2O_3 + h\upsilon \rightarrow g\text{-}C_3N_4@\ ZnO\ (e^-/h^+) - La_2O_3\ (e^-/h^+) \quad (6)$$

$$g\text{-}C_3N_4@\ ZnO\ (e^-/h^+) - La_2O_3\ (e^-/h^+) \rightarrow g\text{-}C_3N_4@\ ZnO\ (e^-) - La_2O_3\ (h^+) \quad (7)$$

$$ZnO\ (e^-) \rightarrow g\text{-}C_3N_4(e^-) \quad (8)$$

$$g\text{-}C_3N_4\ (e^-) + O_2 \rightarrow O_2^{-\cdot} \quad (9)$$

$$O_2^{-\cdot} + H_2O \rightarrow HOO^{\cdot} + HO^- \quad (10)$$

$$HOO^{\cdot} + H_2O \rightarrow H_2O_2 + HO^{\cdot} \quad (11)$$

$$H_2O_2 + g\text{-}C_3N_4\ (e^-) \rightarrow HO^{\cdot} + HO^- \quad (12)$$

$$La_2O_3\ (h^+) + H_2O \rightarrow HO^{\cdot} \quad (13)$$

$$HO^{\cdot}/O_2^{-\cdot} + \text{Organic pollutant} \rightarrow CO_2 + H_2O \quad (14)$$

The hydroxyl and superoxide radicals initiate an attack on the functional groups within the methylene blue [61] dye that contain sulfur and nitrogen. These active species degrade organic contaminants like MB dye and transform them into chemicals that are not hazardous.

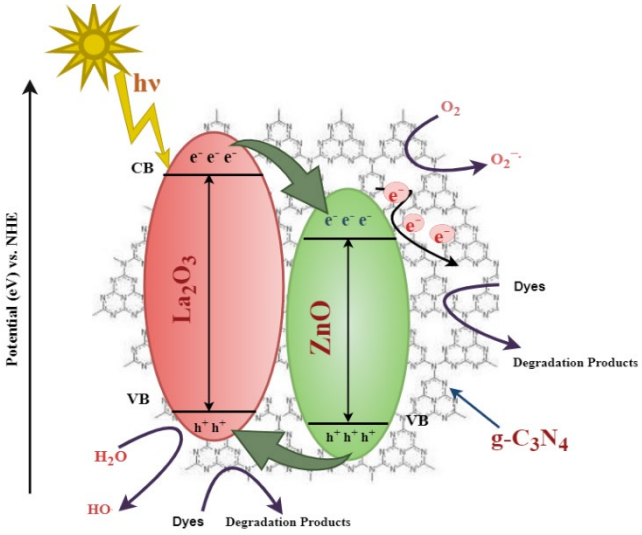

Fig. 13. Illustration in a schematic form of a potential mechanism underlying the photocatalytic activity of nanocomposites made of g-C_3N_4@ZnO/La_2O_3.

3.6.7. Recyclability of Photocatalyst

Reusability and sustainability of the photocatalyst are crucial for real-world applications. Three consecutive cycles of g-C_3N_4@ZnO/La_2O_3 for MB degradation were examined. Each cycle was completed by ultracentrifuging the photocatalyst from the reaction mixture. Following a cycle of washing it in distilled water, it will be heated to dry at 60 °C. The recycling experiment using g-C_3N_4@ZnO/La_2O_3 photocatalyst is illustrated in Figure 14 under the same experimental circumstances as previously stated. After three successive cycles, no significant decline in photocatalytic activity was observed, which is crucial for the photocatalyst's practical uses. After three catalysis cycles, the photocatalyst's catalytic efficiency for the degradation of MB is barely any lower than when it was initially synthesized. The g-C_3N_4@ZnO/La_2O_3 nanocomposite exhibits

excellent stability and reusability. As stated by Cui et al. [62], the noticeable decline in photocatalytic activity may be caused by extreme temperatures and catalyst deficiency during washing. According to the findings, placing ZnO/La_2O_3 in a hybrid structure on g-C_3N_4 protects from leaching and photo-corrosion.

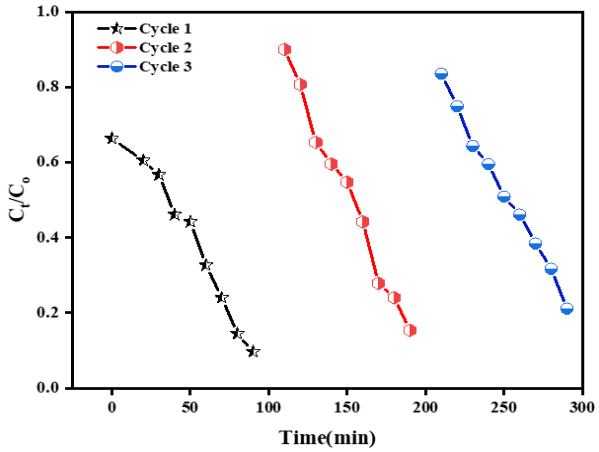

Fig. 14. Photocatalytic recyclability of g-C_3N_4@ZnO/La_2O_3 for three consecutive cycles.

4. Conclusion

This study presents the fabrication of novel ternary photocatalysts, g-C_3N_4@ZnO/La_2O_3 composites, through the co-precipitation and ultrasonication. The nanocomposites' structural and optical characteristics were scrutinized employing UV-Visible and X-ray diffraction (XRD) methodologies, affirming exceptional purity. Moreover, the elemental composition and morphology were analysed via EDX and SEM, respectively. In the context of the degradation process of benzoic acid (BA) and methylene blue dye when subjected to visible light, the photodegradation efficacy of these composites was evaluated through UV-Visible spectroscopy. Incorporating g-C_3N_4 in the composites resulted in enhanced degradation rates of MB dye, with the degradation rate being 90.38% in 120 minutes. The degradation rate of BA was approximately 68.34% when the g-C_3N_4@ZnO/La_2O_3 composite was used. The rate constant also increased with the photodegradation of methylene blue dye. The prepared photocatalysts demonstrated desirable properties, including high stability, degradation ability, and affordability. After three cycles, the g-C_3N_4@ZnO/La_2O_3 composite showed a small decline in photocatalytic activity, demonstrating its stability and efficiency. With their excellent dye removal and regeneration capacity, these nanocomposites offer an efficient, economical, and practical solution for large-scale applications in environmental remediation and wastewater treatment. Overall, the synthesized nanocomposites prove to be suitable photocatalysts for various photocatalytic applications and the treatment of wastewater.

Acknowledgements

The authors express their appreciation to Princess Nourah bint Abdulrahman University Researchers Supporting Project number (PNURSP2025R19), Princess Nourah bint Abdulrahman University, Riyadh, Saudi Arabia. The authors also acknowledge the research grant funded by the Research, Development, and Innovation Authority (RDIA), Kingdom of Saudi Arabia, under grant number (12615-IU-2023-IU-R-2-1-EI).

References

[1] W.S. Koe, J.W. Lee, W.C. Chong, Y.L. Pang, L.C. Sim, Environmental Science and Pollution Research, 27 (2020) 2522-2565; https://doi.org/10.1007/s11356-019-07193-5

[2] M. Ikram, N. Abid, A. Haider, A. Ul-Hamid, J. Haider, A. Shahzadi, W. Nabgan, S. Goumri-Said, A.R. Butt, M.B. Kanoun, Nanoscale Advances, 4 (2022) 926-942; https://doi.org/10.1039/D1NA00802A

[3] M.A. Rauf, S.S. Ashraf, Chemical Engineering Journal, 151 (2009) 10-18; https://doi.org/10.1016/j.cej.2009.02.026

[4] L.V. Thaninki, A. Samson Nesaraj, M. Arunkumar, Iranian Journal of Catalysis, 12 (2022) 315-336.

[5] A. Rafiq, M. Ikram, S. Ali, F. Niaz, M. Khan, Q. Khan, M. Maqbool, Journal of Industrial and Engineering Chemistry, 97 (2021) 111-128; https://doi.org/10.1016/j.jiec.2021.02.017

[6] Y. Guo, P. Qi, Y. Liu, IOP Conference Series: Earth and Environmental Science, 63, 012025, IOP Publishing, UK, 2017; https://doi.org/10.1088/1755-1315/63/1/012025

[7] D. Chen, A.K. Ray, Chemical Engineering Science, 56 (2001) 1561-1570; https://doi.org/10.1016/S0009-2509(00)00383-3

[8] M. Rafatullah, O. Sulaiman, R. Hashim, A. Ahmad, Journal of hazardous materials, 177 (2010) 70-80; https://doi.org/10.1016/j.jhazmat.2009.12.047

[9] Y. Hua, J. Xiao, Q. Zhang, C. Cui, C. Wang, Nanoscale research letters, 13 (2018) 1-9; https://doi.org/10.1186/s11671-018-2476-7

[10] A. Manikandan, E. Manikandan, B. Meenatchi, S. Vadivel, S. Jaganathan, R. Ladchumananandasivam, M. Henini, M. Maaza, J.S. Aanand, Journal of Alloys and Compounds, 723 (2017) 1155-1161; https://doi.org/10.1016/j.jallcom.2017.06.336

[11] J. Lu, I. Batjikh, J. Hurh, Y. Han, H. Ali, R. Mathiyalagan, C. Ling, J.C. Ahn, D.C. Yang, Optik, 182 (2019) 980-985; https://doi.org/10.1016/j.ijleo.2018.12.016

[12] Y. Huo, X. Zhang, Y. Jin, J. Zhu, H. Li, Applied Catalysis B: Environmental, 83 (2008) 78-84; https://doi.org/10.1016/j.apcatb.2008.02.005

[13] V. Kumari, N. Kumar, S. Yadav, A. Mittal, S. Sharma, Materials Today: Proceedings, 19 (2019) 650-657; https://doi.org/10.1016/j.matpr.2019.07.748

[14] M. Mittal, A. Gupta, O. Pandey, Solar Energy, 165 (2018) 206-216; https://doi.org/10.1016/j.solener.2018.03.033

[15] H. Li, B. Fu, H. Huang, S. Wu, J. Ge, J. Zhang, F. Li, P. Qu, Environmental Pollutants and Bioavailability, 34 (2022) 395-406; https://doi.org/10.1080/26395940.2022.2123047

[16] D. Lu, P. Fang, J. Ding, M. Yang, Y. Cao, Y. Zhou, K. Peng, K.K. Kondamareddy, M. Liu, Applied Surface Science, 396 (2017) 185-201; https://doi.org/10.1016/j.apsusc.2016.09.022

[17] K. Choi, T. Kang, S.-G. Oh, Materials Letters, 75 (2012) 240-243; https://doi.org/10.1016/j.matlet.2012.02.031

[18] S. Sakthivel, B. Neppolian, M. Shankar, B. Arabindoo, M. Palanichamy, V. Murugesan, Solar energy materials and solar cells, 77 (2003) 65-82; https://doi.org/10.1016/S0927-0248(02)00255-6

[19] A. Kitai, Luminescent materials and applications, John Wiley & Sons2008; https://doi.org/10.1002/9780470985687

[20] P.-p. Wang, B. Bai, S. Hu, J. Zhuang, X. Wang, Journal of the American Chemical Society, 131 (2009) 16953-16960; https://doi.org/10.1021/ja907043b

[21] C. Bedoya, G.G. Condorelli, S.T. Finocchiaro, A. Di Mauro, D. Atanasio, I. Fragala, L. Cattaneo, S. Carella, Chemical vapor deposition, 12 (2006) 46-53; https://doi.org/10.1002/cvde.200506391

[22] Y. Xie, J. Wu, C. Sun, Y. Ling, S. Li, X. Li, J. Zhao, K. Yang, Materials Chemistry and Physics, 246 (2020) 122846; https://doi.org/10.1016/j.matchemphys.2020.122846

[23] A. Irshad, M.F. Warsi, P.O. Agboola, G. Dastgeer, M. Shahid, Journal of Alloys and Compounds, 902 (2022) 163805; https://doi.org/10.1016/j.jallcom.2022.163805

[24] M. Afshari, M. Dinari, M.M. Momeni, Ultrasonics Sonochemistry, 42 (2018) 631-639; https://doi.org/10.1016/j.ultsonch.2017.12.023

[25] T. Alizadeh, F. Rafiei, Materials Chemistry and Physics, 227 (2019) 176-183; https://doi.org/10.1016/j.matchemphys.2019.01.060

[26] A. Hatamie, P. Jalilian, E. Rezvani, A. Kakavand, A. Simchi, Measurement, 134 (2019) 679-687; https://doi.org/10.1016/j.measurement.2018.10.082

[27] Q. Hao, G. Jia, W. Wei, A. Vinu, Y. Wang, H. Arandiyan, B.-J. Ni, Nano Research, 13 (2020) 18-37; https://doi.org/10.1007/s12274-019-2589-z

[28] N. Rono, J.K. Kibet, B.S. Martincigh, V.O. Nyamori, Critical Reviews in Solid State and Materials Sciences, 46 (2021) 189-217; https://doi.org/10.1080/10408436.2019.1709414

[29] C.H. Hak, L.C. Sim, K.H. Leong, Y.H. Chin, P. Saravanan, IOP conference series: materials science and engineering, IOP Publishing, 2018, pp. 012008; https://doi.org/10.1088/1757-899X/409/1/012008

[30] N. Shaheen, M. Waqas, A. Alazmi, A.A. Alkhudhayri, M. Hasan, M. Shahid, M.F. Warsi, I.A. Alsafari, Materials Chemistry and Physics, 292 (2022) 126754; https://doi.org/10.1016/j.matchemphys.2022.126754

[31] Y. Zhang, Q. Pan, G. Chai, M. Liang, G. Dong, Q. Zhang, J. Qiu, Scientific reports, 3 (2013) 1-8; https://doi.org/10.1038/srep01943

[32] K. Li, F.-Y. Su, W.-D. Zhang, Applied Surface Science, 375 (2016) 110-117; https://doi.org/10.1016/j.apsusc.2016.03.025

[33] C. Ye, J.-X. Li, Z.-J. Li, X.-B. Li, X.-B. Fan, L.-P. Zhang, B. Chen, C.-H. Tung, L.-Z. Wu, ACS catalysis, 5 (2015) 6973-6979; https://doi.org/10.1021/acscatal.5b02185

[34] N. Ramjeyanthi, M. Alagar, D. Muthuraman, Int. J. Interdiscip. Res. Innov., 6 (2018) 389-395.

[35] A.J. Ahamed, P.V. Kumar, Journal of Chemical and Pharmaceutical Research, 8 (2016) 624-628.

[36] Y. Zhao, X. Liang, H. Shi, Y. Wang, Y. Ren, E. Liu, X. Zhang, J. Fan, X. Hu, Chemical Engineering Journal, 353 (2018) 56-68; https://doi.org/10.1016/j.cej.2018.07.109

[37] S. Yan, Z. Li, Z. Zou, Langmuir, 25 (2009) 10397-10401; https://doi.org/10.1021/la900923z

[38] L. Xu, J. Xia, L. Wang, H. Ji, J. Qian, H. Xu, K. Wang, H. Li, European Journal of Inorganic Chemistry, 2014 (2014) 3665-3673; https://doi.org/10.1002/ejic.201402051

[39] R.E. Adam, G. Pozina, M. Willander, O. Nur, Photonics and Nanostructures-Fundamentals and Applications, 32 (2018) 11-18; https://doi.org/10.1016/j.photonics.2018.08.005

[40] K.M. Katubi, A. Jabeen, Z. Alrowaili, M. Al-Buriahi, M. Anwar, A. Manzoor, I. Shakir, M.F. Warsi, Journal of Sol-Gel Science and Technology, 111 (2024) 486-499; https://doi.org/10.1007/s10971-024-06464-z

[41] N. Jayarambabu, B.S. Kumari, K.V. Rao, Y. Prabhu, Int. J. Curr. Eng. Technol, 4 (2014) 3411-3416.

[42] A.R. Noori, To investigate the Effect of Alkaline Earth Metals on Electrochemical Activities of Lanthanum Cobalt Zinc Oxide Cathode Materials, Physics COMSATS University Islamabad Lahore Campus, 2024.

[43] S. Karthikeyan, M. Parthibavarman, M.K. Mohammed, S.H. Mohammed, M. Selvapandiyan, V. Srisuvetha, Chemistry Africa, 5 (2022) 1427-1432; https://doi.org/10.1007/s42250-022-00448-8

[44] Q. Hao, X. Niu, C. Nie, S. Hao, W. Zou, J. Ge, D. Chen, W. Yao, Physical Chemistry Chemical Physics, 18 (2016) 31410-31418; https://doi.org/10.1039/C6CP06122B

[45] M. Irshad, M.M. Ibrahim, S. Siddique, U. Younas, G.A.M. Mersal, S.S. Al-Juaid, A. Irshad, M. Farooq Warsi, Ceramics International, (2025); https://doi.org/10.1016/j.ceramint.2025.02.145

[46] A. Jabeen, H.H. Abd El-Gawad, T.R. Aldhafeeri, M. Sohail, M.F. Warsi, I.A. Alsafari, Ceramics International, (2025); https://doi.org/10.1016/j.ceramint.2025.02.391

[47] P. Sangaiya, R. Jayaprakash, Materials Science in Semiconductor Processing, 85 (2018) 40-51; https://doi.org/10.1016/j.mssp.2018.05.033

[48] A. Jabeen, N.S. Alsaiari, K.M. Katubi, I. Shakir, Z. Alrowaili, M. Al-Buraihi, M.F. Warsi, Journal of Molecular Liquids, 405 (2024) 125066; https://doi.org/10.1016/j.molliq.2024.125066

[49] F. Wu, W. Duan, M. Li, H. Xu, International Journal of Photoenergy, 2018 (2018); https://doi.org/10.1155/2018/7082785

[50] K. Mustofa, Y. Yulizar, A. Saefumillah, D. Apriandanu, IOP Conference Series: Materials Science and Engineering, IOP Publishing, 2020, pp. 012018; https://doi.org/10.1088/1757-899X/902/1/012018

[51] N.A. Putri, V. Fauzia, S. Iwan, L. Roza, A.A. Umar, S. Budi, Applied Surface Science, 439 (2018) 285-297; https://doi.org/10.1016/j.apsusc.2017.12.246

[52] R. Ashna, Y. Yulizar, D. ApriandanuIOP Conference Series: Materials Science and Engineering, IOP Publishing, 2020, pp. 012004; https://doi.org/10.1088/1757-899X/763/1/012004

[53] F.A. Alharthi, A. Ali Alghamdi, H.S. Alanazi, A.A. Alsyahi, N. Ahmad, Catalysts, 10 (2020) 1457; https://doi.org/10.3390/catal10121457

[54] A. Uddin, A. Rauf, T. Wu, R. Khan, Y. Yu, L. Tan, F. Jiang, H. Chen, Journal of Colloid and Interface Science, 602 (2021) 261-273; https://doi.org/10.1016/j.jcis.2021.06.003

[55] M.A. Hanif, J. Akter, M.A. Islam, I. Lee, K.P. Sapkota, S. Shrestha, A. Pandey, N. Gyawali, J.R. Hahn, Journal of Photochemistry and Photobiology A: Chemistry, 431 (2022) 114066; https://doi.org/10.1016/j.jphotochem.2022.114066

[56] H. Bahiraei, S. Azarakhsh, S. Ghasemi, Ceramics International, (2023); https://doi.org/10.1016/j.ceramint.2023.03.240

[57] K.N. Van, V.N.N. Thi, T.P.T. Thi, T.T. Truong, T.L. Le Thi, H.T. Huu, V. Vo, Chemical Physics Letters, 763 (2021) 138191; https://doi.org/10.1016/j.cplett.2020.138191

[58] N. Iqbal, Catalysts, 12 (2021) 15; https://doi.org/10.3390/catal12010015

[59] K. Chaudhary, N. Shaheen, S. Zulfiqar, M.I. Sarwar, M. Suleman, P.O. Agboola, I. Shakir, M.F. Warsi, Binary Synthetic Metals, 269 (2020) 116526; https://doi.org/10.1016/j.synthmet.2020.116526

[60] O.J. Hao, H. Kim, P.-C. Chiang, Critical reviews in environmental science and technology, 30 (2000) 449-505; https://doi.org/10.1080/10643380091184237

[61] J. Fito, K.K. Kefeni, T.T.J.S.o.t.T.E. Nkambule, The potential of biochar-photocatalytic nanocomposites for removal of organic micropollutants from wastewater, 829 (2022) 154648; https://doi.org/10.1016/j.scitotenv.2022.154648

[62] W. Cui, H. Wang, Y. Liang, B. Han, L. Liu, J. Hu, Chemical Engineering Journal, 230 (2013) 10-18; https://doi.org/10.1016/j.cej.2013.03.091